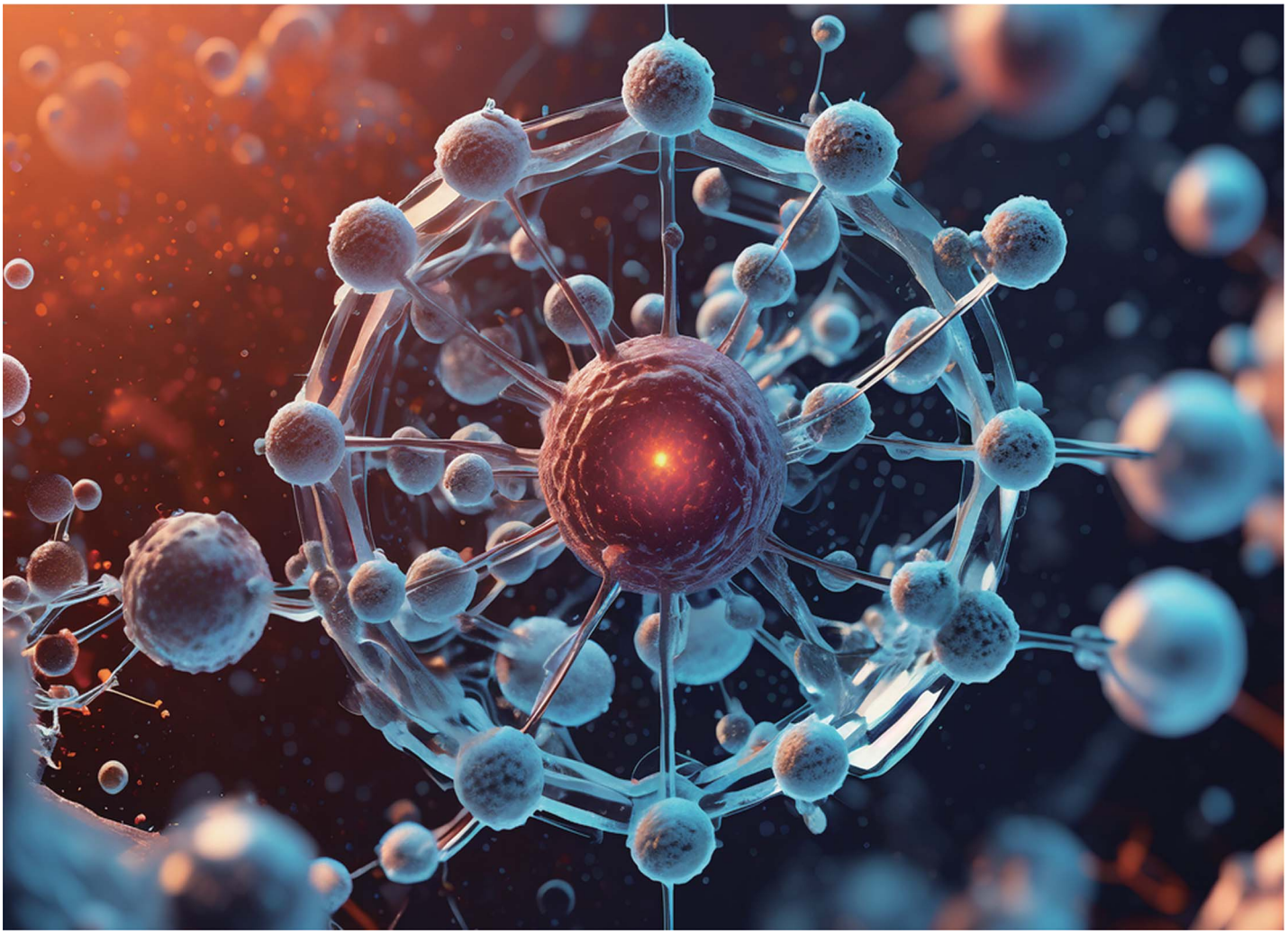

Showcasing research from the laboratory of Professor Cailing Ma, First Affiliated Hospital of Xinjiang Medical University, Xinjiang, China, Obstetrics and Gynecology Center, State Key Laboratory for the Etiology and Prevention of High Incidence Diseases in Central Asia.

Targeted nanotherapy platform mediated tumor-infiltrating CD8⁺ T cell immune function effects for collaborative anti-tumor photothermal immunotherapy for cervical cancer

This study aims to explore novel therapeutic approaches for advanced/recurrent cervical cancer by evaluating the efficacy and superiority of FLIC NPs in immunothermal therapy, with the potential to alter the treatment paradigm for advanced/recurrent cervical cancer. Professor Cailing Ma is dedicated to the diagnosis, treatment, and basic research of gynaecological malignancies.

As featured in:

See Cailing Ma, Chuanshan Zhang *et al.*, *Nanoscale Adv.*, 2024, **6**, 3052.

ROYAL SOCIETY OF CHEMISTRY

rsc.li/nanoscale-advances

Registered charity number: 207890

Nanoscale Advances

ROYAL SOCIETY OF CHEMISTRY

PAPER

View Article Online
View Journal | View Issue

Cite this: *Nanoscale Adv.*, 2024, **6**, 3052

Targeted nanotherapy platform mediated tumor-infiltrating CD8$^+$ T cell immune function effects for collaborative anti-tumor photothermal immunotherapy for cervical cancer

Lei Wang,[a] Jianhuan Chen,[a] Cailing Ma *[a] and Chuanshan Zhang*[b]

Photothermal immunotherapy is an innovative approach to cancer treatment. It combines immunomodulators and photothermal agents, both targeted to the tumor site. This therapy harnesses the heat generated by photothermal conversion to damage tumor cells while simultaneously releasing tumor-associated antigens. This process enhances the anti-tumor immune response of tumor-infiltrating lymphocytes (TILs) within the tumor microenvironment (TME). Photothermal immunotherapy is gaining prominence as a new method for cancer treatment. It is a current focal point in research due to its targeted efficacy, minimal systemic side effects, and reduced risk of treatment resistance. This study employed a thin-film dispersion method to fabricate liposomes (LIPO) as composite drug carriers. Indocyanine green (ICG) for clinical use was utilized as a photothermal agent (PTA), and folate (FA) was employed as a targeting agent for the nano-composite material. We encapsulated the immunoadjuvant CpG ODN within the FA@LIPO@ICG nano-system, resulting in the formation of targeted nanoparticles (NPs) for photothermal immunotherapy (FA@LIPO@ICG@CpG), and assessed the drug encapsulation rate. FA@LIPO@ICG@CpG NPs demonstrated excellent water solubility with an average size ranging from 100 to 200 nm. Furthermore, we investigated the photothermal properties of FA@LIPO@ICG@CpG NPs. Under 808 nm laser irradiation, the photothermal conversion efficiency of FA@LIPO@ICG@CpG NPs reached 39.05%. Subsequently, under 808 nm laser excitation, we conducted an analysis of lymphocyte subpopulations and their functional changes in U14 tumor-bearing mice by using flow cytometry. This treatment approach demonstrated remarkable anti-tumor efficacy. Consequently, FA@LIPO@ICG@CpG NPs hold substantial promise as a novel and promising strategy in cancer therapy.

Received 19th December 2023
Accepted 10th April 2024

DOI: 10.1039/d3na01132a

rsc.li/nanoscale-advances

Introduction

Cervical cancer is a malignancy that poses a significant threat to women's health, ranking as the fourth most common cancer affecting women globally. Current clinical treatment methods for cervical cancer include radiation therapy, chemotherapy, and/or surgical removal. However, these conventional treatments are associated with notable side effects and have certain limitations regarding their effectiveness. Particularly, there is a lack of effective clinical treatments for the cases of recurrence or metastasis. Therefore, there is an urgent need to proactively explore novel and effective treatment modalities for cervical cancer, especially to enhance clinical outcomes for patients with advanced, recurrent, or metastatic cervical cancer.

The development of cervical cancer involves the utilization of various immune evasion mechanisms to evade the body's immune surveillance. As cervical cancer research progresses, immunotherapy can reverse the immune-suppressive microenvironment within the body, thereby improving the body's anti-cancer immune response. Therefore, leveraging immunotherapy to improve the immune microenvironment and simultaneously enhance the functionality of effector T cells may hold the key to advancing cervical cancer immunotherapy. Photothermal therapy (PTT) is an approach that utilizes a photothermal agent (PTA) to generate sufficient heat when exposed to near-infrared light, with the aim of eradicating tumor cells and triggering anti-tumor immune responses.[1–4] PTT is characterized by its high selectivity and minimally invasive nature, making it a promising candidate for effective cervical cancer treatment.[5–9] However, cervical cancer's tumor

[a]*Department of Gynecology, The First Affiliated Hospital of Xinjiang Medical University, State Key Laboratory of Pathogenesis, Prevention and Treatment of High Incidence Diseases in Central Asia, Urumqi 830054, Xinjiang, China. E-mail: hymcl13009661999@126.com*

[b]*Clinical Medicine Institute, The First Affiliated Hospital of Xinjiang Medical University, State Key Laboratory of Pathogenesis, Prevention and Treatment of High Incidence Diseases in Central Asia, Urumqi 830054, Xinjiang, China. E-mail: dashan0518@126.com*

microenvironment (TME) is marked by intricate physiological and pathological immune barriers, and the limited penetration depth of laser light restricts the effectiveness of PTT in treating solid tumors.[10] These challenges hinder PTT from effectively reversing the tumor's immunosuppressive microenvironment and controlling the growth of residual tumor cells. Consequently, the combination of immunotherapy with photothermal treatment holds substantial potential for advancing cervical cancer treatment, offering ample opportunities for research and development.[11–15]

This experiment employed artificially synthesized oligodeoxynucleotides containing CpG motifs (CpG ODNs), designed to be non-methylated, as immunoadjuvants. These CpG ODNs, in conjunction with ICG, a near-infrared photothermal agent, were used to create a targeted immune photothermal nanomaterial known as FA@LIPO@ICG@CpG NPs. We then conducted a comprehensive study on its combined immunotherapy and photothermal treatment effects using a cervical cancer mouse model. The synergy of immunomodulators and PTA, targeted to the tumor site, serves a dual purpose. On the one hand, it enhances the local anti-tumor immune response through the immunoadjuvant effect.[16] On the other hand, upon laser excitation, it generates heat through its photothermal conversion effect, resulting in damage to tumor cells and concurrent release of tumor-associated antigens.[17] This combined action within tumor tissues significantly amplifies the reversal of the immunosuppressive state of tumor-infiltrating lymphocytes (TILs) in the TME.[18] Consequently, it effectively stimulates the anti-tumor immune response of TILs within the TME, ultimately achieving the goal of tumor cell elimination and cancer treatment.[19–23]

FA@LIPO@ICG@CpG NPs exhibit excellent water solubility with an average size ranging from 100 to 200 nm. In this study, the photothermal performance of FA@LIPO@ICG@CpG NPs was investigated, and under 808 nm laser irradiation, the photothermal conversion efficiency of FA@LIPO@ICG@CpG NPs reached 43.7%. Subsequently, the photothermal therapy (PTT) efficacy of FA@LIPO@ICG@CpG NPs was further confirmed using HeLa cells, where the efficiency exceeded 80%. The cellular uptake of FA@LIPO@ICG@CpG NPs was validated through cell confocal experiments, clearly demonstrating the significant internalization of this nanomaterial by cells. Additionally, biocompatibility, targeting, and toxicity analyses of FA@LIPO@ICG@CpG NPs were performed using a C57BL/6 cervical cancer mouse model.[24] These NPs exhibited strong tumor-targeting properties, and no significant *in vivo* toxicity reactions were observed within both 48 hours and 7 days.[25] Subsequent flow cytometry analysis focused on assessing lymphocyte subpopulations and their functional changes in tumor-bearing mice.[26–29] The results indicated that FA@LIPO@ICG@CpG NPs could induce lymphocyte differentiation within the tumor mouse model, enhancing lymphocyte's anti-tumor activity and effectively inhibiting tumor growth. This treatment approach demonstrated remarkable anti-tumor efficacy in tumor-bearing mice.[30] Therefore, photothermal immunotherapy holds great promise as an innovative and promising approach for cancer treatment.

Materials and methods

Materials

Clinical-grade ICG was sourced from Hangzhou Ausia Biotechnology Co., Ltd. Polycarbonate membranes were obtained from Whatman Biochemicals. Soybean phosphatidylcholine (SPC), cholesterol, DOTAP, DSPE-PEG-FA, and PEG with a molecular weight of 2000 were procured from Xi'an Ruixi Biochemical Co., Ltd. CpG oligodeoxynucleotides were acquired from Suzhou Synbio Technologies. Phosphate-buffered saline (PBS) was purchased from Shanghai Hyclone Co., Ltd. Dulbecco's Modified Eagle Medium (DMEM), fetal bovine serum (FBS), and trypsin were sourced from Shanghai Hyclone Co., Ltd. The FITC Cell Apoptosis Detection Kit was obtained from BD Biosciences. The Cell Counting Kit-8 (CCK-8) was provided by Biosharp Life Sciences. RBC Lysis buffer (10×), fixation buffer, and intracellular staining permeabilization wash buffer (10×) were obtained from Biolegend, USA. Percoll was supplied by Cytiva. PBS (pH 7.2, 10×) was procured from Gibco. Collagenase IV, hyaluronic acid, DNase I, and RPMI 1640 were sourced from Solarbio Life Sciences. The Cell Stimulation Cocktail (plus protein transport inhibitors) and TM Foxp3/transcription factor staining buffer set were obtained from eBioscience, and NaN3 was purchased from Beijing Borunlaite Science & Technology Co., Ltd. Flow cytometry antibodies, including NK1.1, CD3, CD4, CD8, CD69, CD25, CD44, CD62L, CD11C, MHC-II, IFN-γ, TNF-α, Ki67, IL-6, IL-10, Foxp3, and TGF-β, were acquired from Biolegend, USA. Deionized water was used throughout all experimental procedures.

Preparation of FA@LIPO@ICG@CpG NPs

The preparation of FA@LIPO@ICG@CpG NPs involves two steps. Step 1: SPC, 1,2-dioleoyl-3-trimethylammonium-propane (DOTAP), distearoyl phosphatidyl ethanolamine-polyethylene glycol-folate (DSPE-PEG-FA), ICG, and cholesterol were combined in the following mass ratio: 0% : 10% : 15% : 10% : 15%. The mixture was stirred at room temperature (1200 rpm) overnight resulting in the formation of FA@LIPO@ICG NPs. Step 2: CpG oligonucleotides (1.5 mg, 10%) were dissolved in citrate buffer (50 mM citrate, pH = 4) containing 25% ethanol. This solution was slowly added to the previously synthesized FA@LIPO@ICG NP liposome system. 100 W ultrasonic shaking was performed for 15 minutes, and the resulting solution was filtered through a liposome extruder (100 nm filter membrane). The filtrate was subsequently dialyzed using a nanodialysis device (polycarbonate membrane, pore size 10 nm) to obtain the final product, FA@LIPO@ICG@CpG NPs. In the experimental material, the molecular weight of ICG is 775 g mol^{-1}. In every 5 mg of FA@LIPO@ICG@CpG NP freeze-dried powder, there is 1 mg of FA@LIPO@ICG@CpG NPs and 0.045 mg of ICG, with a drug loading rate of 4.5% and an encapsulation rate of 90%. Additionally, there is 0.034 mg of CpG ODN with an encapsulation rate of 85.7%.

Characterization of the FA@LIPO@ICG@CpG NPs

To accurately determine the loading capacity (LC) and encapsulation efficiency (EE) of ICG within FA@LIPO@ICG@CpG

NPs, the following steps were undertaken: firstly, the UV absorption spectrum of free ICG at 808 nm was recorded, generating a standard absorbance curve of ICG (correlating absorbance intensity with concentration). The supernatants obtained from the two-step preparation process were used for measurements. The fluorescence and absorbance values of the supernatants collected after each washing step were determined using a Shimadzu UV-1800 spectrophotometer. The ICG content in the supernatant was quantified based on the corresponding ICG absorbance curve at 808 nm. The quantity of ICG loaded into FA@LIPO@ICG@CpG NPs was derived from the absorbance values. Subsequently, the LC and EE of ICG within FA@LIPO@ICG@CpG NPs were calculated using the following equations:

$$\mathrm{LC} = \frac{W_{\text{feeding drug}} - W_{\text{drug in supernatant}}}{W_{\text{composite NPs}}} \times 100\% \quad (1)$$

$$\mathrm{EE} = \frac{W_{\text{feeding drug}} - W_{\text{drug in supernatant}}}{W_{\text{feeding drug}}} \times 100\% \quad (2)$$

Further quantification of the LC and EE of CpG ODN in FA@LIPO@ICG@CpG NPs was performed using Quant-iT Picogreen dsDNA quantification assay, yielding values of 3.4% and 85.7%, respectively.

Dynamic light scattering (DLS)

Using different solvents including water, PBS, and culture medium, solutions A, B, and C of FA@LIPO@ICG@CpG NPs were prepared with a concentration of 20 μ mL^{-1}. The particle size to DLS mode (temperature = 25 °C and angle = 90°) was adjusted to measure the hydrodynamic diameter of FA@LIPO@ICG@CpG NPs for one week. The polydisperse index (PDI) is an important indicator of the dispersion degree of the reaction solution, and the formula for calculating the PDI is as follows: $PDI = SD^2/Z^2$, where SD is the standard deviation of DLS and Z is the average value of DLS.

Photothermal performance of FA@LIPO@ICG@CpG NPs

The photothermal performance is a crucial indicator of the PTT efficacy of FA@LIPO@ICG@CpG NPs. An in-depth assessment of the photothermal performance of FA@LIPO@ICG@CpG NPs was conducted. Initially, six different concentrations of FA@LIPO@ICG@CpG NPs (6.25, 12.5, 25, 50, 100 and 200 μg mL^{-1}) were analyzed. Under 808 nm laser irradiation at a power density of 1 W cm^{-2}, temperature changes were monitored using an infrared thermal imager (FOTRIC, Shanghai Heat Image Technology Co., Ltd). The temperature of the solution was recorded every 30 seconds for a total of 15 minutes, aiming to observe and analyze how the temperature of FA@LIPO@ICG@CpG NPs changed with varying concentrations. Additionally, FA@LIPO@ICG@CpG NPs (at a concentration of 200 μg mL^{-1}, calculated based on ICG content) were exposed to an 808 nm laser at different power densities (0.1 W cm^{-2}, 0.2 W cm^{-2}, 0.4 W cm^{-2}, 0.6 W cm^{-2}, 0.8 W cm^{-2}, and 1 W cm^{-2}). Temperature changes were monitored using an infrared thermal imager, recording the solution's temperature every 30 seconds for 15 minutes. Furthermore, the photothermal performance of four different substances (ICG, LIPO@ICG, FA@LIPO@ICG, and FA@LIPO@ICG@CpG NPs) was assessed under identical concentrations (calculated based on an ICG content of 200 μg mL^{-1}, with water as the solvent) and exposed to an 808 nm laser at a power density of 1 W cm^{-2}. Temperature changes were monitored using an infrared thermal imager, recording the solution's temperature every 30 seconds for a total of 15 minutes to evaluate the photothermal performance of these various substances. Moreover, FA@LIPO@ICG@CpG NPs underwent five consecutive cycles of heating and cooling. An 808 nm laser (power density of 1 W cm^{-2}) was applied continuously to the solution for 15 minutes to induce heating, followed by stopping the irradiation to allow natural cooling for an additional 15 minutes. This constituted one cycle, and five cycles were consecutively performed to further observe and analyze the photothermal stability of FA@LIPO@ICG@CpG NPs.

The equation for calculating the photothermal conversion efficiency is as follows:

$$\eta = \frac{M_{\mathrm{D}} C_{\mathrm{D}} (T_{\max} - T_{\max,\text{water}})}{\tau_{\mathrm{s}} I \left(1 - 10^{-A_{808}}\right)} \times 100\% \quad (3)$$

Cell culture and cytotoxicity analysis

The HeLa cells were seeded into a 96-well plate at a density of 5 × 10^3 cells per well (in 200 μL of cell culture medium) and then incubated in a humidified incubator for 24 hours at 37 °C with 5% CO_2. Following this, HeLa cells were exposed to various concentrations of FA@LIPO@ICG@CpG NPs (0 μg mL^{-1}, 6.25 μg mL^{-1}, 12.5 μg mL^{-1}, 25 μg mL^{-1}, 50 μg mL^{-1}, 100 μg mL^{-1}, and200 μg mL^{-1}, dissolved in 200 μL of complete cell culture medium) for 24 hours. Cell viability was assessed using Cell Counting Kit-8 assay (Dojindo). The cell viability of HeLa cells treated with 0 μg mL^{-1} FA@LIPO@ICG@CpG NPs was considered as 1.0, and the viability of cells in other wells was normalized to this reference value. Each concentration was tested in triplicate, and measurements were taken using a Model 680 Microplate reader (168-1000XC).

Near infrared fluorescence imaging of cells

HeLa cells were initially seeded into 35 mm glass-bottom culture dishes at a density of 3 × 10^5 cells per well, with 1 mL of complete cell culture medium, and then incubated for 12 hours at 37 °C with 5% CO_2. Following the removal of the upper culture medium, HeLa cells were divided into two groups as follows: (1) control group (1 mL of complete cell culture medium) and (2) FA@LIPO@ICG@CpG NP group (200 μg mL^{-1}, calculated based on ICG content, dissolved in 1 mL of complete cell culture medium). The cells were further incubated for 2 hours, and then the upper culture medium was discarded. Afterward, HeLa cells were rinsed three times with 1× PBS (pH = 7.4) and subjected to DAPI staining (10 μg mL^{-1}) in the dark for 20 minutes. Following the removal of the upper staining solution, HeLa cells were washed three times with 1× PBS (pH =

7.4) and supplemented with 1 mL of DMEM. The cellular uptake of FA@LIPO@ICG@CpG NPs was observed using a confocal laser scanning microscope (CLSM) (Leica, TCS-SP5) under static conditions. Images of HeLa cells were captured using excitation/emission wavelengths of 405/480 nm and 640/810 nm to assess the uptake of FA@LIPO@ICG@CpG NPs.

Once again, HeLa cells were cultured in 35 mm glass-bottom Petri dishes (cell preparation, as mentioned earlier). The HeLa cells were divided into four groups: (1) control group (1 mL of complete culture medium), (2) laser group (1 mL of complete culture medium), (3) FA@LIPO@ICG@CpG NP group (200 μg mL^{-1}, calculated based on ICG content, dissolved in 1 mL of complete culture medium), and (4) FA@LIPO@ICG@CpG NPs + laser group (808 nm laser with a power density of 1 W cm^{-2}, continuous irradiation for 10 minutes). After 2 hours of incubation followed by laser treatment, the upper culture medium was removed, and the HeLa cells were washed three times with 1× PBS (pH = 7.4). The cells were then stained with Calcein AM (4 mM) and PI (10 μg mL^{-1}) in the dark for 15 minutes. After washing the cells, 1 mL of DMEM was added, and HeLa cell images were captured using a confocal laser scanning microscope (CLSM) (Leica, TCS-SP5) with excitation wavelengths of 490 nm, 520 nm, and 640 nm to assess the effects of FA@LIPO@ICG@CpG NP treatment on HeLa cells.

In vitro photothermal therapy analysis

Cell apoptosis induced by PTT of FA@LIPO@ICG@CpG NPs was assessed using flow cytometry. Initially, HeLa cells were seeded into 6-well plates at a density of 1×10^5 cells per well. Subsequently, HeLa cells were divided into four groups: (1) control group, (2) laser group, (3) FA@LIPO@ICG@CpG NP group (200 μg mL^{-1}, calculated based on ICG content, dissolved in 1 mL of complete cell culture medium), and (4) FA@LIPO@ICG@CpG NPs + laser group (incubated for 2 hours followed by continuous irradiation with an 808 nm laser at a power density of 1 W cm^{-2} for 10 minutes). All groups of cells were washed twice with PBS. All cells were stained with PI (5 μL) and Annexin V-FITC (5 μL) in the presence of binding buffer for 15 minutes. Subsequently, 500 μL of 1× PBS was added to remove the antibodies (centrifuged at 1000 rpm for 5 minutes). Flow cytometry (BD LSRII, FACS Calibur) was then used to assess the apoptotic status of the cells.

Hemolysis assay

Whole blood was obtained from healthy C57BL/6 mice using the retro-orbital bleeding method, collected in anticoagulant tubes containing sodium citrate. The blood was centrifuged at 3000 rpm for 15 minutes to obtain blood cells, which were then prepared into a 4% red blood cell suspension to assess the hemolytic rate of the nanoparticles. 2 mL of 0.9% NaCl solution (negative control), 2 mL of different concentrations of FA@LIPO@ICG@CpG NPs dissolved in 0.9% NaCl solution (6.25 μg mL^{-1}, 12.5 μg mL^{-1}, 25 μg mL^{-1}, 50 μg mL^{-1}, 100 μg mL^{-1}, and 200 μg mL^{-1}), and 2 mL of ultrapure water (ddH_2O, positive control) were mixed with 100 μL of blood cells separately. The mixtures were then incubated at 37 °C for 1 hour, followed by centrifugation at 3000 rpm for 15 minutes to observe any hemolysis in each group. The supernatant was collected for spectrophotometric analysis at 540 nm (triplicate measurements for each group, calculating the standard deviation).

The hemolysis rate calculation formula is as follows:

$$\text{Hemolysis rate}(\%) = \frac{OD_{\text{sample test group}} - OD_{\text{negative control group}}}{OD_{\text{sample test group}} - OD_{\text{positive control group}}} \times 100\%$$

If the hemolysis rate of the FA@LIPO@ICG@CpG nanomaterial is below 4.5%, it is consistent with the requirements of the medical hemolysis experiment; if it is above 4.5%, then it does not meet the requirements.

Drug release kinetics of FA@LIPO@ICG@CpG NPs

FA@LIPO@ICG@CpG NPs, ICG, and CpG (2 mL, 200 μg mL^{-1}, calculated based on an ICG content of 200 μg mL^{-1}) were placed in a dialysis bag (molecular weight 12 000), clamped at both ends, and immersed in 50 mL PBS (pH = 7.4, 37 °C) at 37 °C. Two sets were prepared, one without laser irradiation and the other with 808 laser (1 W cm^{-2}) irradiation for 10 minutes. PBS solutions were collected at 10 minutes, 20 minutes, 30 minutes, 2 h, 12 h, and 24 h, and 48 h. ICG concentration was measured using UV/visible spectrophotometry, and CpG concentration was measured using a Quant-iT Picogreen dsDNA quantitation kit to calculate the cumulative release rates of ICG and CpG. The experiment was repeated 3 times, and the average values were taken.

Biosafety assays

To assess the safety of FA@LIPO@ICG@CpG NPs, five healthy female KM mice were selected. They received intravenous injections of FA@LIPO@ICG@CpG NPs (200 μg mL^{-1}, at a dose of 30 μg kg^{-1}). The survival of these mice was monitored at 12 hours, 24 hours, 3 days, and 7 days post injection. Major organs, including the heart, liver, spleen, lungs, and kidneys, were collected for histopathological examination using H&E staining. The morphology of the tissue organ was observed under an inverted digital microscope (Leica).

Establishment of a cervical tumor model, tumor-targeting NIR fluorescence imaging and metabolism analysis

Female C57BL/6 mice (4–6 weeks old, obtained from Beijing Charles River Laboratories) were subcutaneously injected with 1×10^7 U14 cells in 200 μL on the right upper limb. Tumor growth took approximately 2 weeks. Every other day, measurements were taken of the animal's body weight and tumor size. Tumor volume was calculated using the formula: volume = (length × $width^2$)/2. When the tumor volume reached 50 mm^3, the U14 tumor-bearing mice were divided into four groups (n = 5 for each group): (1) control group (PBS group), (2) CpG group, (3) FA@LIPO@ICG + laser group (200 μg mL^{-1}, calculated based on ICG content), and (4) FA@LIPO@ICG@CpG NPs + laser group (200 μg mL^{-1}, calculated based on ICG content). Each group

underwent different therapeutic interventions on days 1, 4, and 7.

To assess the tumor-targeting ability and metabolism of FA@LIPO@ICG@CpG NPs, 9 female C57BL/6 tumor-bearing mice (with tumor volumes reaching 50 mm^3) were divided into three groups ($n = 3$ for each group): (1) control group (PBS group), (2) ICG group (200 μg mL^{-1}), and (3) FA@LIPO@ICG@CpG NP group (200 μg mL^{-1}, calculated based on ICG content). ICG and FA@LIPO@ICG@CpG NP solutions (10 mg kg^{-1}, calculated based on ICG content) were administered to the tumor-bearing mice *via* tail vein injection. Fluorescence imaging was performed using a fluorescence imaging system (745 nm laser excitation and 840 nm emission) at 0 hours, 2 hours, 12 hours, 24 hours, 48 hours, and 72 hours. After 72 hours, the organs (heart, liver, spleen, lungs, kidneys, and tumor) were collected from the mice, and near-infrared fluorescence imaging was conducted for evaluation.

In vivo photothermal analysis

9 female C57BL/6 mice were divided into three groups ($n = 3$ for each group): (1) control group (PBS group): mice received a tail vein injection of PBS. (2) ICG group (200 μg mL^{-1}): mice received a tail vein injection of an ICG solution (10 mg kg^{-1}, calculated based on ICG content). (3) FA@LIPO@ICG@CpG NP group (200 μg mL^{-1}): mice received a tail vein injection of FA@LIPO@ICG@CpG NP solution (10 mg kg^{-1}, based on ICG content). The mice were anesthetized using inhaled isoflurane gas and exposed to 808 nm laser irradiation at a power density of 1 W cm^{-2}. Temperature changes within the tumors were monitored using an infrared thermal imaging system (FOTRIC, Shanghai Heat Image Technology Co., Ltd). Tumor temperature was recorded every 30 seconds for a total monitoring period of 15 minutes, allowing for the observation and analysis of the photothermal effects of FA@LIPO@ICG@CpG NPs.

Isolation of tumor-infiltrating lymphocytes in mice

Isolation of tumor-infiltrating lymphocytes: to isolate TILs, mice were euthanized by cervical dislocation and tumor tissues were collected. The tumor tissues were minced and transferred into a 15 mL centrifuge tube. Digestive enzymes (0.2% collagenase, 0.01% hyaluronidase, and 0.002% DNAse I) were added for thorough mixing. After digestion, the cell pellet was resuspended in 80% Percoll and subjected to gradient centrifugation. The supernatant was then discarded, and a red blood cell lysis buffer was used for a 12 minute lysis. Subsequently, the cells were washed with PBS buffer, resuspended to a final volume of 1 mL, and counted for subsequent antibody labeling experiments.

Lymphocyte phenotype detection

The collected lymphocytes were divided into individual tubes, each containing 1×10^6 cells. The cells were then resuspended in a blocking solution containing α-CD16/32 and incubated at 4 °C for 30 minutes. Following this, the cells were labeled with antibodies against NK1.1, CD3, CD4, CD8, CD19, CD69, CD44, CD62L, CD11C, and MHC-II, and incubated in the dark at 4 °C for an additional 30 minutes. After washing with PBS, the cell suspension was passed through a 200-mesh/25.4 mm nylon mesh to remove impurities and transferred into flow cytometry tubes for subsequent analysis on the machine.

Cytokine secretion detection

The collected lymphocytes were transferred to 1.5 mL EP tubes at a concentration of 2×10^6 cells per tube. They were washed with PBS, and the supernatant was discarded. The cells were then resuspended in RPMI 1640 culture medium containing a 1× cocktail and stimulated in a CO_2 incubator for 4 hours. After stimulation, the cells were labeled with antibodies against NK1.1, CD3, CD8, and CD44, following the previously described steps. After a PBS wash, the cells were resuspended in 250 μL of fixation buffer and incubated in the dark at 4 °C for 30 minutes. Each tube was then centrifuged at 400×*g* for 6 minutes (centrifuge radius at 8.4 cm), followed by centrifugation at 8500×*g* for 3 minutes (centrifuge radius at 8.4 cm). The cells were washed twice with PBS. Subsequently, 30 μL of internal control antibodies for IFN-γ, TNF-α, TGF-β, IL-6, and IL-10, prepared in 1× permeabilization wash buffer, were added to each tube, mixed, and incubated in the dark at 4 °C for 45 minutes. After washing with PBS, the cell suspension was filtered through a 200-mesh/25.4 mm nylon mesh to remove impurities and transferred into flow cytometry tubes for analysis on the machine.

Statistical analysis

The Mann–Whitney *U* test was conducted using Origin 9.1 (OriginLab, Northampton, USA). Fluorescence images were analyzed with Image J. Statistical analyses were carried out using SPSS 26.0. Continuous data are presented as mean ± standard deviation ($x \pm s$). Differences between two groups were assessed using the *t*-test, while differences among multiple groups were analyzed using one-way analysis of variance (ANOVA). Pairwise comparisons were adjusted using the Bonferroni correction (for homogeneity of variances) or the Dunnett T3 test (for heterogeneity of variances). A p-value < 0.05 was considered statistically significant. GraphPad Prism 10.3 software was utilized for data visualization.

Ethical approval and patient-informed consent

This study was approved by the Ethics Committee of the First Affiliated Hospital of Xinjiang Medical University (approval number: (20 191 113-08)) and did not involve patient informed consent.

Results and discussion

Preparation and characterization of FA@LIPO@ICG@CpG NPs

FA@LIPO@ICG NPs were synthesized by using a mass ratio of SPC, DOTAP, DSPE-PEG-FA, ICG, and cholesterol. This synthesis resulted in the formation of FA@LIPO@ICG NPs (Scheme 1). Folic acid serves as a targeting agent for these nanomaterials, facilitating the specific delivery of anti-tumor

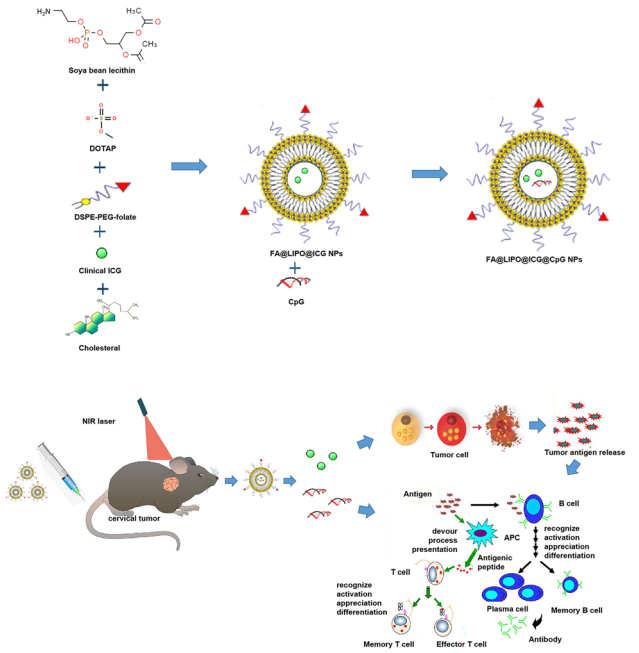

Scheme 1 Synthesis of FA@LIPO@ICG@CpG NPs and the process of photothermal immunotherapy.

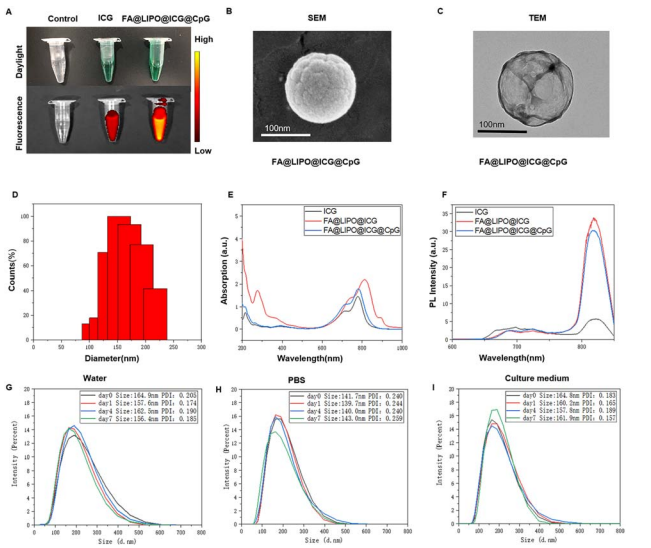

Fig. 1 (A) Dispersions of PBS, ICG aqueous solution, and FA@LIPO@ICG@CpG NP aqueous solution (concentration: 200 μg mL^{-1}). (B) SEM image of FA@LIPO@ICG@CpG NPs (scale: 100 nm). (C) TEM image of FA@LIPO@ICG@CpG NPs (scale: 100 nanometers). (D) Particle size of FA@LIPO@ICG@CpG NPs. (E) Absorption spectra of the three substances, ICG (black line), FA@LIPO@ICG NPs (red line), and FA@LIPO@ICG@CpG NPs (blue line) in aqueous dispersion. (F) Fluorescence properties of the three substances, ICG (black line), FA@LIPO@ICG NPs (red line), and FA@LIPO@ICG@CpG NPs (blue line) in aqueous dispersion. (G–I) DLS and polydispersity index (PDI) results of FA@LIPO@ICG@CpG NPs.

drugs. The use of liposomes as nanomaterial carriers enhances the uptake efficiency of these nanodrugs by tumor cells, promoting their cellular absorption. ICG not only plays a role in PTT but also possesses reliable biocompatibility. Additionally, CpG ODN, through its binding with TLR-9, promotes the anti-tumor immune response of TILs. We determined the LC and EE of ICG in FA@LIPO@ICG@CpG NPs using absorbance spectroscopy and quantified the LC and EE of CpG ODN using a Quant-iT Picogreen dsDNA quantification kit.

As depicted in Fig. 1A, the ICG aqueous solution (200 μg mL^{-1}) exhibits a color of bright green, while the FA@LIPO@ICG@CpG NP solution (200 μg mL^{-1}, dissolved in deionized water) appears as a yellow-green emulsion. This coloration is due to the presence of folic acid, which imparts a yellow hue, and the dispersion of liposomes in water, resulting in an emulsion-like appearance. In Fig. 1B and C, TEM and SEM images, respectively, reveal that the synthesized FA@LIPO@ICG@CpG NPs are spherical in shape with an average particle size of 150 nanometers. DLS analysis confirms an average particle size of 150 nm for FA@LIPO@ICG@CpG NPs, as illustrated in Fig. 1D. The UV-vis absorption spectra of ICG NPs, FA@LIPO@ICG NPs, and FA@LIPO@ICG@CpG NPs are presented in Fig. 1E. ICG (black line) exhibits an absorption peak at 780 nm. Notably, FA@LIPO@ICG NPs (red line) and FA@LIPO@ICG@CpG NPs (blue line) show a redshift in their absorption peaks. This shift demonstrates the successful incorporation of ICG, FA, LIPO, and CpG. Fig. 1F displays the fluorescence spectra of ICG NPs, FA@LIPO@ICG NPs, and FA@LIPO@ICG@CpG NPs in their water-dispersed solutions. ICG (black line), FA@LIPO@ICG NPs (red line), and FA@LIPO@ICG@CpG NPs (blue line) exhibit peaks in the near-infrared range at 820 nm, emitting near-infrared fluorescence signals. The fluorescence signal of FA@LIPO@ICG NPs (red line) and FA@LIPO@ICG@CpG NPs is stronger than that of ICG, attributed to the liposome encapsulation of ICG, which enhances its fluorescence signal. Therefore, FA@LIPO@ICG NPs and FA@LIPO@ICG@CpG NPs are enveloped within a liposomal structure on their surfaces. Further calculations indicate that the LC and EE of ICG in FA@LIPO@ICG@CpG NPs are 4.5% and 90%, respectively. The LC and EE of CpG ODN in FA@LIPO@ICG@CpG NPs are determined using a Quant-iT Picogreen dsDNA quantification kit, resulting in values of 3.4% and 85.7%, respectively.

Dynamic light scattering (DLS)

As shown in Fig. 1G–I, the results of particle size (DLS) and polydispersity index (PDI) as shown in the graph indicate that in solution A, the diameter of FA@LIPO@ICG@CpG NPs is approximately 164.9 nm, 157.6 nm, 162.5 nm, and 156.4 nm (day 0, day 1, day 4, and day 7). In solution B, the diameter of FA@LIPO@ICG@CpG NPs is approximately 141.7 nm, 139.7 nm, 140.0 nm, and 143.0 nm (day 0, day 1, day 4, and day 7). In solution C, the diameter of FA@LIPO@ICG@CpG NPs is approximately 164.8 nm, 160.2 nm, 157.8 nm, and 161.9 nm (day 0, day 1, day 4, and day 7). The uniform and stable distribution of the diameter of FA@LIPO@ICG@CpG NPs in different solutions over one week indicates good stability, further confirming the successful preparation of FA@LIPO@ICG@CpG NPs in different solvents.

Evaluation of photothermal performance

The photothermal properties of the FA@LIPO@ICG NPs and FA@LIPO@ICG@CpG NPs synthesized in this experiment have been significantly enhanced. As shown in Fig. 2A, when near-infrared laser irradiation was applied for 15 minutes to aqueous dispersions of water, ICG NPs, FA@LIPO@ICG NPs, and FA@LIPO@ICG@CpG NPs (calculated based on ICG content, with ICG concentration at 200 μg mL^{-1}), the temperature of the ICG NP solution increased by 25 °C, while the FA@LIPO@ICG NP solution exhibited a temperature increase of 33 °C, and the FA@LIPO@ICG@CpG NP solution showed a temperature increase of 30 °C. This clearly demonstrates that the photothermal performance of FA@LIPO@ICG NPs and FA@LIPO@ICG@CpG NPs surpasses that of ICG. As shown in Fig. 2B and E, when different concentrations of FA@LIPO@ICG@CpG NP aqueous solutions (6.25, 12.5, 25, 50, 100, and 200 μg mL^{-1}, calculated based on ICG content) were irradiated with an 808 nm laser for 15 minutes, the results demonstrated that the rate and extent of temperature increase in FA@LIPO@ICG@CpG NP solution increased with higher concentrations. This indicates that the photothermal performance of FA@LIPO@ICG@CpG NPs is positively correlated with concentration. In Fig. 2C, an 808 nm near-infrared laser with different power densities (0.1 W cm^{-2}, 0.2 W cm^{-2}, 0.4 W cm^{-2}, 0.8 W cm^{-2}, and 1 W cm^{-2}) was used to irradiate FA@LIPO@ICG@CpG NP solution. With the increase in laser power density, the photothermal performance of FA@LIPO@ICG@CpG NPs also improved. In Fig. 2D, to evaluate the photothermal stability of FA@LIPO@ICG@CpG NPs, the solution was irradiated with an 808 nm laser (1 W cm^{-2}) for 15 minutes, with 15 seconds of irradiation followed by 15 seconds of cooling, repeated for 5 cycles. During these 5 cycles of irradiation, there were no significant differences in temperature changes between each cycle, indicating that FA@LIPO@ICG@CpG NPs exhibit excellent photothermal stability. As shown in Fig. 2E, after 5 cycles of near-infrared irradiation, FA@LIPO@ICG@CpG NPs displayed good photostability. The photothermal conversion efficiency (η) of FA@LIPO@ICG@CpG NPs was calculated to be 39.05%, which is higher than that of ICG NPs (15.28%). Therefore, FA@LIPO@ICG@CpG NPs exhibit photothermal effects and can serve as a nanomaterial for cancer treatment.

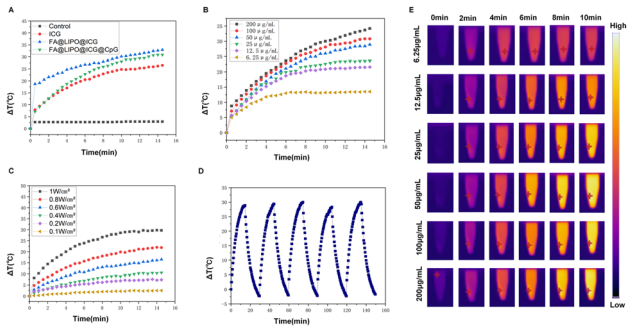

Fig. 2 *In vitro* photothermal experiments; (A) temperature increase in various solutions including water, ICG NPs, FA@LIPO@ICG NPs, and FA@LIPO@ICG@CpG NPs (calculated based on ICG content, ICG concentration at 200 μg mL^{-1}) after 15 minutes of near-infrared laser irradiation; (B) temperature increase in FA@LIPO@ICG@CpG NP solutions of different concentrations after 15 minutes of near-infrared laser irradiation; (C) temperature increase in FA@LIPO@ICG@CpG NPs (200 μg mL^{-1}, calculated based on ICG content) under near-infrared laser irradiation with varying power densities for 15 minutes; (D) temperature changes in FA@LIPO@ICG@CpG NP water-dispersed solution (200 μg mL^{-1}, calculated based on ICG content) during 5 cycles of near-infrared laser irradiation/cooling. Excitation: 808 nm and power density: 1 W cm^2; (E) infrared thermal images of FA@LIPO@ICG@CpG NP water-dispersed solution at different concentrations under near-infrared laser irradiation.

Cytotoxicity analysis, cellular uptake and cellular photothermal evaluation

As depicted in Fig. 3A, the biocompatibility of FA@LIPO@ICG@CpG NPs was assessed through a CCK-8 cell cytotoxicity analysis. HeLa cells were incubated separately with water-dispersed solutions of ICG NPs, FA@LIPO@ICG NPs, and

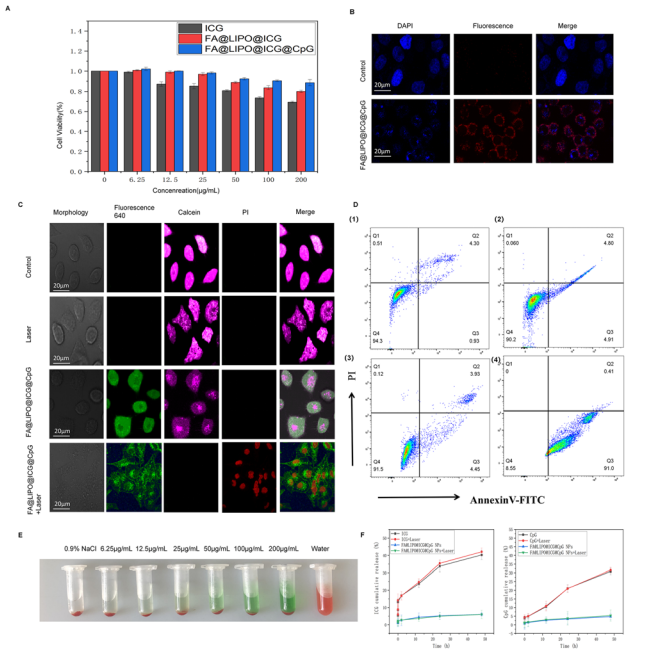

Fig. 3 (A) Cell viability of HeLa cells after co-incubation with ICG, FA@LIPO@ICG NPs, and FA@LIPO@ICG@CpG NPs at different concentrations for 24 hours (the data are presented as mean ± SD, $N = 3$ per group, NS indicates no significance, $*p < 0.05$, and $**p < 0.01$). (B) Fluorescence images of HeLa cells incubated with or without FA@LIPO@ICG@CpG NPs using CLSM. Fluorescence images of HeLa cells incubated with or without FA@LIPO@ICG@CpG NPs. $\lambda_{em} = 800–1000$ nm, $\lambda_{ex} = 405$ nm (DAPI), and $\lambda_{ex} = 640$ nm (ICG). Scale bar: 20 μm. (C) CLSM images of HeLa cells in different treatment groups. Scale bar: 20 μm, (D) Flow cytometry analysis of HeLa cells in different treatment groups (as described above), stained with Annexin V-FITC and PI. (E) Mouse blood *in vitro* hemolysis assay (in the hemolysis test, the red area represents complete hemolysis, and the hemolysis is normalized to the DI-water positive control, with a hemolysis rate of 100%). (F) The *in vitro* cumulative release rates of ICG from FA@LIPO@ICG@CpG NPs at different time points (excitation: 808 nm and power density: 1 W cm^{-2}), as well as the *in vitro* cumulative release rates of CpG from FA@LIPO@ICG@CpG NPs at different time points (excitation: 808 nm and power density: 1 W cm^{-2}).

FA@LIPO@ICG@CpG NPs for 24 hours. It was observed that HeLa cells incubated with FA@LIPO@ICG@CpG NPs maintained a cell viability of over 80%. This indicates that FA@LIPO@ICG@CpG NPs have low cytotoxicity and are biologically safe. As illustrated in Fig. 3B, to assess the uptake capability of HeLa cells for FA@LIPO@ICG@CpG NPs, HeLa cells were co-incubated with FA@LIPO@ICG@CpG NPs (at a concentration of 200 μg mL^{-1}, calculated based on ICG content) for 2 hours. Subsequently, the cell nuclei of HeLa cells were stained with DAPI (in blue), and fluorescence was observed in both the blue channel (DAPI, E_x = 405 nm) and the red channel (FA@LIPO@ICG@CpG NPs, E_x = 640 nm) using CLSM. This observation confirms the excellent biocompatibility of FA@LIPO@ICG@CpG NPs and their ability to be taken up by HeLa cells.

In Fig. 3C, the photothermal therapeutic effect of FA@LIPO@ICG@CpG NPs was observed through CLSM images of HeLa cells. In Group A (control group), live cells and dead cells were stained with Hoechst and PI, respectively, and no dead cells were observed. In Group B (808 nm laser irradiation only), no dead cells were observed. In Group C (FA@LIPO@ICG@CpG NPs only, 200 μg mL^{-1}, calculated based on ICG content), live cells were visible, and the intracellular uptake of FA@LIPO@ICG@CpG NPs was observed (λ_{ex} = 640 nm). In Group D (FA@LIPO@ICG@CpG NPs, 200 μg mL^{-1}, calculated based on ICG content, and 808 nm laser irradiation at a power density of 1 W cm^{-2} for 10 minutes), almost all HeLa cells stained positive for PI under 808 nm laser irradiation, indicating cell death. Furthermore, flow cytometry was used to confirm the photothermal therapeutic effect of FA@LIPO@ICG@CpG NPs, as shown in Fig. 3D. In Group B (laser only) and Group C (FA@LIPO@ICG@CpG NPs, 200 μg mL^{-1}, calculated based on ICG content), there were only a small number of apoptotic cells (Q2 late apoptotic cells and Q3 early apoptotic cells). In Group D (FA@LIPO@ICG@CpG NPs, 200 μg mL^{-1}, calculated based on ICG content, and 808 nm laser irradiation at a power density of 1 W cm^{-2} for 10 minutes), late apoptotic cells (Q2: 0.41%) and early apoptotic cells (Q3: 91.0%) together accounted for more than 80% of the total apoptotic cells.

As shown in Fig. 3E, the hemolysis ability of FA@LIPO@ICG@CpG NPs was analyzed by a hemolysis experiment, and the hemolysis rates of each group were 0.83%, 0.86%, 0.87%, 0.90%, 0.90%, and 0.93%, among which the hemolysis rates of different concentrations of FA@LIPO@ICG@CpG NP solution are all less than 4.5%, indicating that FA@LIPO@ICG@CpG NPs did not cause significant hemolysis. The results indicate that FA@LIPO@ICG@CpG NPs have high biocompatibility and biosafety, which is beneficial for future clinical translation. The hemolytic ability of FA@LIPO@ICG@CpG NPs was compared in the hemolysis test, and the results showed that FA@LIPO@ICG@CpG NPs did not cause obvious hemolysis. This indicates that FA@LIPO@ICG@CpG NPs have high biocompatibility and safety, suitable for intravenous systemic administration, and conducive to future clinical translation.

The *in vitro* drug release characteristics of ICG and CpG from FA@LIPO@ICG@CpG NPs under near-infrared 808 nm laser irradiation for 10 minutes (1 W cm^{-2}) at pH = 7.4 and 37 °C in PBS solution were studied. As shown in Fig. 3F, free ICG rapidly diffused from the dialysis bag, reaching a release rate plateau within 48 h, accounting for approximately 40.25 ± 2.68% of the total ICG. In contrast, ICG from FA@LIPO@ICG@CpG NPs exhibited slow release, with a cumulative release rate of only 6.03 ± 1.03% within 48 h. After laser irradiation, the cumulative release rates of free ICG and FA@LIPO@ICG@CpG NPs were 42.03 ± 2.18% and 5.99 ± 3.36%, respectively. Free CpG quickly diffused from the dialysis bag, achieving a release rate of approximately 30.82 ± 1.94% within 48 h. Meanwhile, CpG from FA@LIPO@ICG@CpG NPs exhibited slow release, with a cumulative release rate of 4.78 ± 1.84% within 48 h. After laser irradiation, the cumulative release rates of free CpG and FA@LIPO@ICG@CpG NPs were 31.55 ± 1.62% and 4.89 ± 3.24%, respectively. The results indicate that FA@LIPO@ICG@CpG NPs can slow down the release of ICG and CpG, thereby enhancing the photothermal stability of FA@LIPO@ICG@CpG NPs.

In summary, FA@LIPO@ICG@CpG NPs demonstrated good biocompatibility and exhibited a strong photothermal therapeutic effect. The experimental results provide a solid foundation for subsequent animal PTT experiments.

Photothermal targeting, biodistribution analysis and anti-tumor efficacy

Twenty C57BL/6 tumor-bearing mice with tumor volumes reaching 50 mm^3 were selected for photothermal experiments to assess the photothermal effect of FA@LIPO@ICG@CpG NPs in U14 cell-bearing mice. The mice were randomly divided into four groups (n = 4): Group A: control (PBS); Group B: ICG aqueous solution (200 μg mL^{-1}); Group C: FA@LIPO@ICG NPs (200 μg mL^{-1}, calculated based on ICG content); Group D: FA@LIPO@ICG@CpG NPs (200 μg mL^{-1}, calculated based on ICG content). Each group received intravenous injections of the respective drugs, followed by 10 minutes of irradiation (808 nm, 1 W cm^{-2}). In the control group (Group A), the temperature at the tumor site increased to 32 °C, while in Group B (ICG), it increased to 34 °C. In contrast, the mice treated with FA@LIPO@ICG NPs and FA@LIPO@ICG@CpG NPs experienced a rapid increase in tumor site temperature, reaching 49 °C and 51 °C, respectively (Fig. 4A and B). This elevated temperature was sufficient to destroy tumor cells. Subsequently, the therapeutic efficacy of photothermal immunotherapy was evaluated in 20 mice with tumors of approximately the same volume (50 mm^3). They were randomly divided into four groups (n = 4): Group A: control (PBS); Group B: CpG (200 μg mL^{-1}); Group C: FA@LIPO@ICG + laser (200 μg mL^{-1}, calculated based on ICG content, 808 nm laser irradiation at a power density of 1 W cm^{-2} for 10 minutes); Group D: FA@LIPO@ICG@CpG NPs + laser (200 μg mL^{-1}, calculated based on ICG content) combined with laser irradiation (808 nm laser irradiation at a power density of 1 W cm^{-2} for 10 minutes). After treatment, observations were made for 14 days. It was observed that the tumor volumes in Groups A and B continued to show a significant increasing trend, while Group C showed some inhibitory effect on the

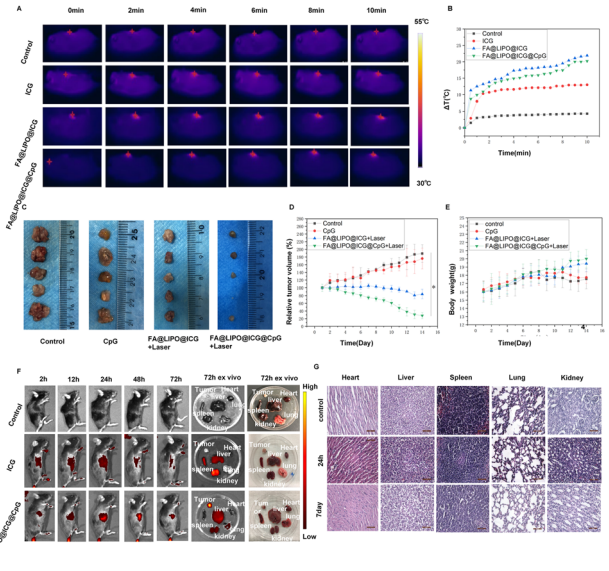

Fig. 4 Evaluation of anti-tumor effects. (A) Infrared thermal imaging of U14 cell-bearing C57BL/6 mice following near-infrared irradiation (808 nm, 1 W cm^{-2}, and 10 minutes). (B) Corresponding temperature change curves for Fig. 5A. (C) Schematic representation of tumor dissection 14 days after various interventions in different groups. (D) Changes in relative tumor volume in different groups 14 days after treatment. Data are presented as mean ± SD (n = 5, ***p < 0.001 between two groups). (E) Changes in the body weight of mice in each group over the course of 14 days. (F) Near-infrared fluorescence imaging at different time points (2 hours, 12 hours, 24 hours, 48 hours, and 72 hours) following intravenous drug administration in different groups of mice: Group A: control (PBS), Group B: ICG (1.5 mg kg^{-1}), and Group C: FA@LIPO@ICG@CpG NPs (1.5 mg kg^{-1}). (G): Examination of major organs (heart, liver, spleen, lungs, and kidneys) at 24 hours and 7 days after intravenous injection of FA@LIPO@ICG@CpG NPs. Scale bar: 12.5 μm.

tumor tissue. In Group D, tumor growth was significantly suppressed (Fig. 4D). Fig. 4C depicts an anatomical schematic of the tumors 14 days after various interventions in different groups, Group A: control (PBS); Group B: CpG (200 μg mL^{-1}); Group C: FA@LIPO@ICG + laser (200 μg mL^{-1}, calculated based on ICG content, 808 nm laser irradiation at a power density of 1 W cm^{-2} for 10 minutes); Group D: FA@LIPO@ICG@CpG NPs + laser (200 μg mL^{-1}, calculated based on ICG content) combined with laser irradiation (808 nm, 1 W cm^{-2}, and 10 minutes).

The changes in the body weight of mice during treatment and observation are shown in Fig. 4E. It can be observed that the body weight of mice in Groups A and B did not increase significantly. In Group C, after drug treatment alone, there was a slight increase in mouse body weight. In Group D, after photothermal immunotherapy, there was a significant increase in mouse body weight. These results indicate that FA@LIPO@ICG@CpG NPs can serve as an effective treatment for cervical cancer.

FA@LIPO@ICG@CpG NPs were intravenously injected into tumor-bearing mice, and a near-infrared fluorescence imaging system was employed to observe the distribution and metabolic behavior of the nanomaterials. To ascertain the tumor-targeting capabilities of these nanomaterials, near-infrared fluorescence signals at the tumor site were continuously monitored. As depicted in Fig. 4F, mice from different treatment groups were observed at 2 hours, 12 hours, 24 hours, 48 hours, and 72 hours following the intravenous administration of the substances. The fluorescence distribution within the mice, as well as the fluorescence signals at the tumor site, was assessed. As illustrated, mice of Group C exhibited maximum near-infrared fluorescence intensity at the tumor site at the 24 hour mark, which continued strongly until 48 hours, gradually diminishing thereafter. After 72 hours post injection, major organs (liver, lungs, spleen, kidneys, heart, and tumor) were excised and imaged using a near-infrared fluorescence imaging system to assess the intensity of the fluorescence signal. Notably, Group C showed strong near-infrared fluorescence emission in the tumor tissue, moderate emission in the liver, and weaker emission in the kidneys. In Group B, strong near-infrared fluorescence emission was observed in the liver, kidneys, and spleen. Conversely, the control group, treated with PBS, exhibited no detectable fluorescence signals. These results substantiate the tumor-targeting capability and near-infrared fluorescence properties of FA@LIPO@ICG@CpG NPs.

The toxicity of FA@LIPO@ICG@CpG NPs was evaluated using C57BL/6 mice. Mice were intravenously injected with FA@LIPO@ICG@CpG NPs (1.5 mg kg^{-1}). Major organs (heart, liver, spleen, lungs, and kidneys) were harvested at 24 hours and 7 days, followed by H&E staining to assess whether FA@LIPO@ICG@CpG NPs caused any pathological damage to the mouse organs. As shown in Fig. 4G, there was no evident drug-induced toxicity or inflammatory lesions observed in the organs of the mice. This indicates that FA@LIPO@ICG@CpG NPs do not harm the internal organs of mice and exhibit a certain degree of biocompatibility, making them a potential photothermal immunotherapy agent for cervical cancer.

Changes in the proportion of tumor-infiltrated mDC and $CD8^+$ T cells in mice

The mice were divided into four groups (n = 4): Group A: control (PBS), Group B: CpG (200 μg mL^{-1}), Group C: FA@LIPO@ICG + laser (200 μg mL^{-1}, calculated from ICG content, 808 nm laser irradiation at a power density of 1 W cm^{-2} for 10 minutes), Group D: FA@LIPO@ICG@CpG NPs + laser (200 μg mL^{-1}, calculated from ICG content) plus laser irradiation (808 nm, 1 W cm^{-2}, and 10 minutes). After 14 days of different treatments, the proportions of tumor-infiltrating mDCs (mature dendritic cells) subpopulations in Groups B, C, and D mice increased to (2.50 ± 0.56)%, (3.16 ± 1.60)%, and (3.50 ± 0.77)%, respectively. These proportions were higher than the (0.90 ± 0.24)% observed in Group A (F = 5.986, P < 0.05), as shown in Scheme 2 and Fig. 5A. In the four groups of mice after different intervention treatments, there were no significant differences in the proportions of tumor-infiltrating $CD8^+$ T cell subpopulations, which were (34.25 ± 5.71)%, (39.53 ± 2.12)%, (35.18 ± 3.12)%, and (34.00 ± 3.18%), respectively (F = 1.863, P > 0.05), as depicted in Scheme 2 and Fig. 5B. However, in mice of Group D, the proportion of activated $CD8^+$ T cells ($CD69^+CD8^+$ T cells) in tumor infiltration increased to (7.16 ± 1.75)%, which was higher than the (4.59 ±

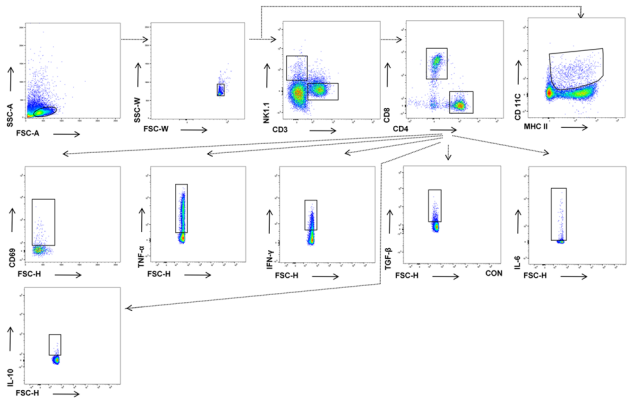

Scheme 2 Gating process for tumor-infiltrating mDC and $CD8^+$ T cell subpopulations.

0.83)% in Group A and (3.78 ± 0.50)% in Group B ($F = 4.524$, $P < 0.05$), as illustrated in Scheme 2 and Fig. 5C. As shown in Fig. 5D, further analysis of the proportions of $CD8^+$ TN, $CD8^+$ Tcm, and $CD8^+$ Tem cells in tumor-infiltrating $CD8^+$ T cells revealed a significant decrease in the proportion of $CD8^+$TN cells in tumor-infiltrating $CD8^+$ T cells in Groups C and D, down to (2.89 ± 3.43)% and (2.15 ± 2.00)%, respectively. These proportions were higher than the (11.30 ± 9.97)% in Group A ($F = 3.053$, $P < 0.05$). Additionally, the proportion of $CD8^+$ Tcm cells in tumor-infiltrating $CD8^+$ T cells in Group D significantly increased to (5.97 ± 2.24)%, which was higher than the (2.41 ± 1.09)% in Group A ($F = 1.845$, $P < 0.05$). Meanwhile, there was an increasing trend in the proportion of $CD8^+$ Tem cells in tumor-infiltrating $CD8^+$ T cells in Groups C and D, which were (44.88 ± 18.54)% and (52.88 ± 24.41)%, respectively, and higher than the (34.85 ± 8.37)% in Group A ($F = 1.768$, $P > 0.05$).

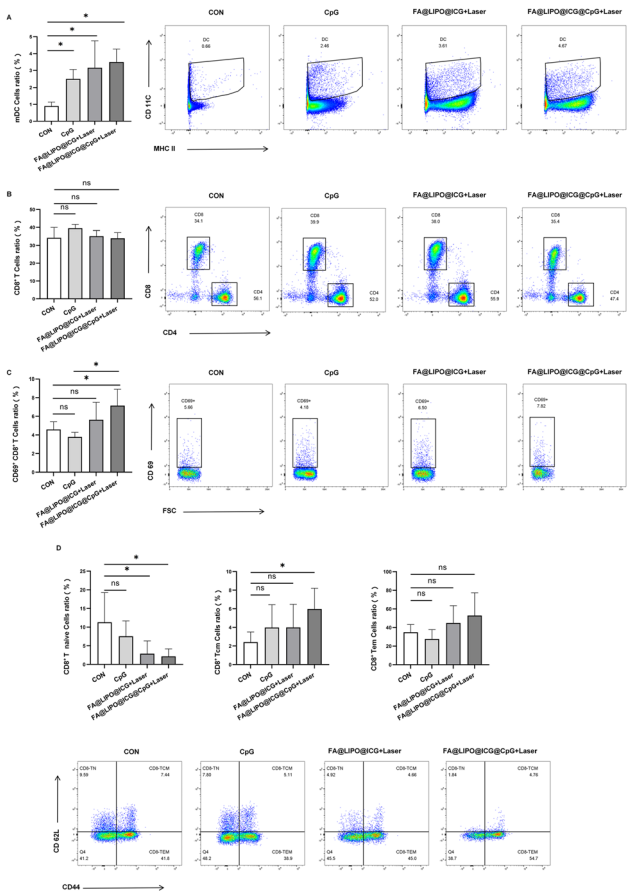

Fig. 5 (A) Proportions of tumor-infiltrating mDC. (B) The proportion of activated $CD8^+$ T cells ($CD69^+CD8^+$ T cells) in tumor. (C) $CD8^+$ T cell subpopulations ($CD69^+CD8^+$ T cells) in cervical cancer mouse models with different interventions. (D) Proportions of $CD8^+$ TN, $CD8^+$ Tcm, and $CD8^+$ Tem cells in tumor-infiltrating $CD8^+$ T cells in cervical cancer mouse models with different interventions.

Changes of cytokines secreted by $CD8^+$ T cells in different groups of mice with tumor infiltration

Four groups of mice ($n = 4$) were divided as follows: Group A, the control group (PBS); Group B, treated with CpG (200 μg mL^{-1}); Group C, subjected to FA@LIPO@ICG + laser treatment (200 μg mL^{-1}, calculated based on ICG content, 808 nm laser irradiation, power density of 1 W cm^{-2}, and 10 minutes); Group D, treated with FA@LIPO@ICG@CpG NPs + laser (200 μg mL^{-1}, calculated based on ICG content) along with laser irradiation (808 nm, power density of 1 W cm^{-2}, and 10 minutes).

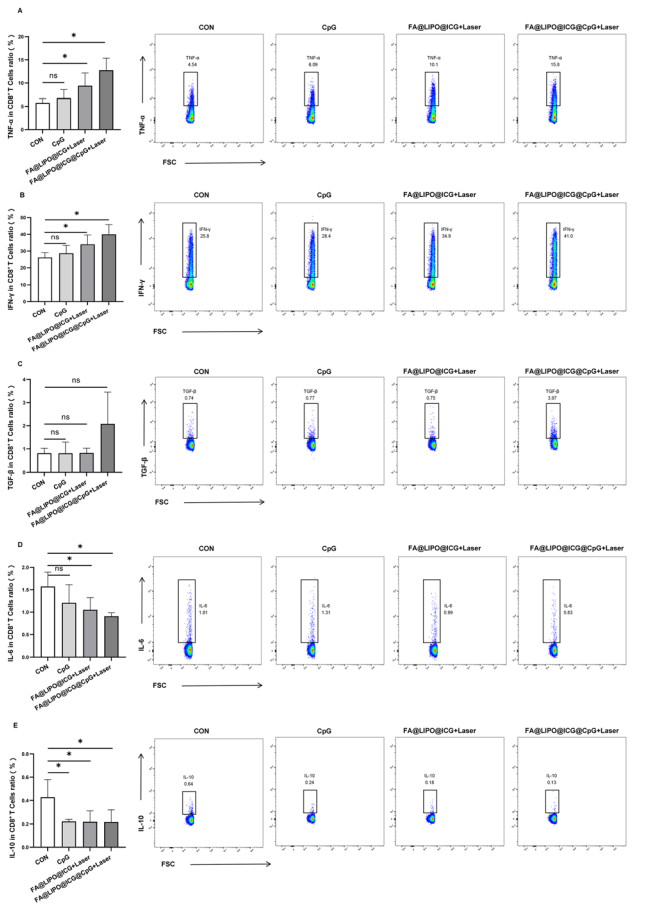

Fig. 6 (A–E) Alterations in cytokine secretion by tumor-infiltrating $CD8^+$ T cells in the cervical cancer mouse models subjected to various interventions.

After 14 days of different treatments, as illustrated in Fig. 6A–E, the secretion of cytokines TNF-α, IFN-γ, TGF-β, IL-6, and IL-10 by tumor-infiltrating $CD8^+$ T cells was analyzed. The results revealed that in Groups C and D, the proportion of TNF-α secretion by tumor-infiltrating $CD8^+$ T cells significantly increased, reaching (9.41 ± 2.75)% and (12.75 ± 2.61)%, respectively, which was higher than that in Group A [(5.74 ± 0.92)%] ($F = 8.472$, $P < 0.05$) (Fig. 6A). Similarly, in Groups C and D, the proportion of IFN-γ secretion by tumor-infiltrating $CD8^+$ T cells significantly rose, reaching (34.00 ± 5.65)% and (40.00 ± 5.84)%, respectively, surpassing that in Group A [(26.20 ± 2.95)%] ($F = 6.137$, $P < 0.05$) (Fig. 6B). In contrast, there was no significant change in the proportion of TGF-β secretion by tumor-infiltrating $CD8^+$ T cells in Groups B and C, which was (0.81 ± 0.49)% and (0.82 ± 0.20)%, respectively, as compared to Group A [(0.81 ± 0.21)%] ($F = 2.920$, $P > 0.05$). In Group D, the proportion of TGF-β secretion by tumor-infiltrating $CD8^+$ T cells slightly increased, measuring (0.81 ± 0.49)% compared to Group A (Fig. 6C). Furthermore, in Groups C and D, the proportion of IL-6 secretion by tumor-infiltrating $CD8^+$ T cells significantly decreased, measuring (1.05 ± 0.27)% and (0.91 ± 0.08)%, respectively, which was lower than that in Group A [(1.57 ± 0.32)%] ($F = 3.767$, $P < 0.05$) (Fig. 6D). Lastly, the proportion of IL-10 secretion by tumor-infiltrating $CD8^+$ T cells significantly decreased in Groups B, C, and D, measuring (0.22 ± 0.17)%, (0.22 ± 0.09)%, and (0.21 ± 0.10)%, respectively, compared to Group A [(0.43 ± 0.15)%] ($F = 4.088$, $P < 0.05$) (Fig. 6E).

Conclusions

This study has synthesized a novel immuno-photothermal nanomaterial, FA@LIPO@ICG@CpG NPs. FA@LIPO@ICG@CpG NPs exhibit biocompatibility and demonstrate excellent photothermal performance under 808 nm laser irradiation. CLSM images reveal that FA@LIPO@ICG@CpG NPs can be taken up by HeLa cells, generating fluorescence signals within the cells. Cell toxicity analysis confirms the low cytotoxicity of FA@LIPO@ICG@CpG NPs. Additionally, Biocompatibility and toxicity experiments show that FA@LIPO@ICG@CpG NPs possess biological safety and stability. No significant toxic reactions are observed both 24 hours and 7 days after the introduction of FA@LIPO@ICG@CpG NPs into the biological system.[31] Subsequently, under the combined intervention of FA@LIPO@ICG@CpG NPs and 808 nm laser irradiation, tumors in cervical cancer-bearing mice notably decreased in size.[32]

This study conducted an in-depth analysis of the impact of photothermal immunotherapy on $CD8^+$ T cells within the TME of cervical cancer-bearing mice.[33] This study has revealed that all three treatment methods, including immunotherapy, PTT, and the combined approach of immunotherapy and PTT, can effectively increase the proportion of mDC cells (activated dendritic cells) within the TME. Following this, we further investigated the variations in $CD8^+$ T cell subpopulations among the different treatment groups. The research unveiled that PTT and photothermal immunotherapy can reduce the proportion of $CD8^+$ TN ($CD8^+$ Naive T cells). However, photothermal immunotherapy can additionally boost the proportion of $CD8^+$ Tcm ($CD8^+$ central memory T cells). $CD8^+$ Tcm cells possess long-term memory and have the capacity to migrate back to lymph nodes, where they receive re-stimulation from antigens. This enables them to exert sustained anti-tumor functions in subsequent anti-tumor immune responses, indicating that the TME within the body suppresses secondary anti-tumor immune responses during the initiation and development of tumors, consequently fostering continuous tumor growth. The study also scrutinized the functional alterations in tumor-infiltrating $CD8^+$ T cells across the various treatment groups. It was found that the $CD69^+CD8^+$ T cell subpopulation, when activated, can secrete a substantial amount of cytokines, playing a pivotal role in anti-tumor immune processes. The results of this study suggest that the ability of $CD8^+$ T cell subpopulations to secrete TNF-α and IFN-γ is significantly heightened in the PTT and photothermal immunotherapy groups. Conversely, their ability to secrete IL-6 and IL-10 is diminished. This implies the existence of an immunosuppressive response within the TME, which hinders the function of tumor-infiltrating $CD8^+$ T cells. Consequently, these $CD8^+$ T cells assume an immunosuppressive state, resulting in immune evasion by tumor cells and the promotion of tumor growth. By externally enhancing the immune functionality of $CD8^+$ T cells within the TME, the body's capacity to mount anti-tumor immune responses and enhance tumor-killing capabilities can be rapidly heightened.

In summary, this study underscores the significant therapeutic potential of the photothermal immunotherapy nanomaterial FA@LIPO@ICG@CpG NPs in anti-tumor treatments, pointing to promising prospects for future development.[34,35]

Conflicts of interest

The authors report no conflicts of interest in this work.

Acknowledgements

This work was funded by the National Natural Science Foundation of China (82260613 and 62071059), Fundamental Research Funds for the Central Universities and State Key Laboratory of Pathogenesis, Prevention and Treatment of High Incidence Diseases in Central Asia Fund (SKL-HIDCA-2022-GJ1, SKLHIDCA-2022-2, ZYYD2022B06, ZYYD2023A09, and SKLHIDCA-2019) and special funds for the central government to guide local science and technology development (ZYYD2023A09). The authors would like to thank Professor Cailing Ma for her critical review and thank Dr Chuanshan ZHANG for his help with graphic figures.

Notes and references

1 Z. Feng, X. Yu, M. Jiang, L. Zhu, Y. Zhang, W. Yang, W. Xi, G. Li and J. Qian, *Theranostics*, 2019, **9**, 5706–5719.
2 F. Wang, J. Zhu, Y. Wang and J. Li, *Nanomaterials*, 2022, **12**, 1656.

3 S. Anand, T. A. Chan, T. Hasan and E. V. Maytin, *Pharmaceuticals*, 2021, **14**, 447.
4 M. Chang, Z. Hou, M. Wang, C. Li and J. Lin, *Adv. Mater.*, 2021, **33**, e2004788.
5 R. Guo, S. Wang, L. Zhao, Q. Zong, T. Li, G. Ling and P. Zhang, *Biomaterials*, 2022, **282**, 121425.
6 Y. Zhang, G. Zhang, G. Wang and L. Wu, *Wiley Interdiscip. Rev.: Nanomed. Nanobiotechnol.*, 2021, **13**, e1717.
7 X. Huang, Y. Lu, M. Guo, S. Du and N. Han, *Theranostics*, 2021, **11**, 7546–7569.
8 Y. Zhao, X. Liu, X. Liu, J. Yu, X. Bai, X. Wu, X. Guo, Z. Liu and X. Liu, *Front. Immunol.*, 2022, **13**, 955920.
9 W. S. Yun, J. H. Park, D. K. Lim, C. H. Ahn, I. C. Sun and K. Kim, *Cancers*, 2022, **14**, 2044.
10 C. Kong and X. Chen, *Int. J. Nanomed.*, 2022, **17**, 6427–6446.
11 C. G. Alves, R. Lima-Sousa, B. L. Melo, A. F. Moreira, I. J. Correia and D. de Melo-Diogo, *Pharmaceutics*, 2022, **14**, 1015.
12 F. Wang, J. Zhu, Y. Wang and J. Li, *Nanomaterials*, 2022, **12**, 1656.
13 C. Xu, Y. Jiang, Y. Han, K. Pu and R. Zhang, *Adv. Mater.*, 2021, **33**, e2008061.
14 L. Tang, A. Zhang, Z. Zhang, Q. Zhao, J. Li, Y. Mei, Y. Yin and W. Wang, *Cancer Commun.*, 2022, **42**, 141–163.
15 Z. Chen, H. Pan, Y. Luo, T. Yin, B. Zhang, J. Liao, M. Wang, X. Tang, G. Huang, G. Deng, M. Zheng and L. Cai, *Small*, 2021, **17**, e2007494.
16 H. Liu, Y. Mei, Q. Zhao, A. Zhang, L. Tang, H. Gao and W. Wang, *Pharmaceutics*, 2021, **13**, 1344.
17 Y. Liu, E. Chorniak, R. Odion, W. Etienne, S. K. Nair, P. Maccarini, G. M. Palmer, B. A. Inman and T. Vo-Dinh, *Nanophotonics*, 2021, **10**, 3295–3302.
18 P. Liu, M. Ye, Y. Wu, L. Wu, K. Lan and Z. Wu, *Cancer Med.*, 2023, **12**, 3201–3221.
19 Z. R. Stephen and M. Zhang, *Adv. Healthcare Mater.*, 2021, **10**, e2001415.
20 C. M. Castelló, M. T. de Carvalho, A. F. Bakuzis, S. G. Fonseca and M. P. Miguel, *Vet. Comp. Oncol.*, 2022, **20**, 752–766.
21 P. McKernan, N. A. Virani, G. N. F. Faria, C. G. Karch, R. Prada Silvy, D. E. Resasco, L. F. Thompson and R. G. Harrison, *Nanoscale Res. Lett.*, 2021, **16**, 9.
22 W. Xu, C. Pang, C. Song, J. Qian, S. Feola, V. Cerullo, L. Fan, H. Yu and V. P. Lehto, *Acta Biomater.*, 2022, **152**, 473–483.
23 T. Y. Huang, G. L. Huang, C. Y. Zhang, B. W. Zhuang, B. X. Liu, L. Y. Su, J. Y. Ye, M. Xu, M. Kuang and X. Y. Xie, *Front. Chem.*, 2020, **8**, 1.
24 V. Yasothamani and R. Vivek, *J. Mater. Chem. B*, 2022, **10**, 6392–6403.
25 A. Y. Lin, B. Choi, T. Sim, E. Yang, H. Choi, A. Behdad, D. H. Kim and L. I. Gordon, *Blood Adv.*, 2022, **6**, 4581–4592.
26 I. C. Miller, A. Zamat, L. K. Sun, H. Phuengkham, A. M. Harris, L. Gamboa, J. Yang, J. P. Murad, S. J. Priceman and G. A. Kwong, *Nat. Biomed. Eng.*, 2021, **5**, 1348–1359.
27 J. Nam, S. Son, K. S. Park and J. J. Moon, *Adv. Ther.*, 2021, **4**, 2100093.
28 Y. Yang, M. Xu, Z. Wang, Y. Yang, J. Liu, Q. Hu, L. Li and W. Huang, *J. Mater. Chem. B*, 2021, **9**, 2613–2622.
29 N. M. Muñoz, C. Dupuis, M. Williams, K. Dixon, A. McWatters, J. Zhang, S. Pavuluri, A. Rao, D. G. Duda, A. Kaseb and R. A. Sheth, *Sci. Rep.*, 2022, **12**, 14449.
30 B. Zhou, Q. Wu, M. Wang, A. Hoover, X. Wang, F. Zhou, R. A. Towner, N. Smith, D. Saunders, J. Song, J. Qu and W. R. Chen, *J. Chem. Eng.*, 2020, 396.
31 Y. Cheng, Q. Chen, Z. Guo, M. Li, X. Yang, G. Wan, H. Chen, Q. Zhang and Y. Wang, *ACS Nano*, 2020, **14**, 15161–15181.
32 B. Zhuang, T. Chen, Y. Huang, Z. Xiao and Y. Jin, *Acta Pharm. Sin. B*, 2022, **12**, 1447–1459.
33 J. Cano-Mejia, A. Shukla, D. K. Ledezma, E. Palmer, A. Villagra and R. Fernandes, *Transl. Oncol.*, 2020, **13**, 100823.
34 Y. Han, H. Pan, W. Li, Z. Chen, A. Ma, T. Yin, R. Liang, F. Chen, Y. Ma, Y. Jin, M. Zheng, B. Li and L. Cai, *Adv. Sci.*, 2019, **6**, 1900251.
35 L. Zhang, J. Zhang, L. Xu, Z. Zhuang, J. Liu, S. Liu, Y. Wu, A. Gong, M. Zhang and F. Du, *J. Nanobiotechnol.*, 2021, **19**(1), 142.